



# TEXTURE AND MICROSTRUCTURE EVOLUTION DURING COLD ROLLING OF A STRIP CAST AND OF A HOT ROLLED AUSTENITIC STAINLESS STEEL

D. RAABE

Institut für Metallkunde und Metallphysik, RWTH Aachen, Kopernikusstr. 14, 52056 Aachen, Germany

(Received 19 December 1995; accepted 5 June 1996)

**Abstract**—The microstructure and texture evolution of a strip cast and of a hot rolled austenitic stainless steel (18% Cr, 8.5% Ni) during cold rolling was studied (maximum thickness reduction  $\Delta d/d_0 = 80\%$ ). The microstructure of the hot band was homogeneous through the sheet thickness, except that in the centre layer a small volume fraction of martensite appeared. The hot band texture revealed a through-thickness gradient which was discussed in terms of the shear distribution during hot rolling. The microstructure of the cast strip showed globular grains with martensite in the centre layer and blocks of austenitic dendrites in the other layers. The formation of martensite was attributed to the deformation of the solidified films in the rolling gap. The strip cast sample revealed a weak texture fibre close to  $\{001\}\langle uvw \rangle$  which was interpreted in terms of growth selection during solidification. During cold rolling in both types of samples the volume fraction of martensite increased up to  $\sim 50$  vol.% (80% reduction). The cold rolling texture of the austenite was in both cases characterized by  $\{011\}\langle 211 \rangle$  and  $\{011\}\langle 100 \rangle$ . The cold rolling texture of the hot band was stronger than that of the strip cast sample which was attributed to the influence of the starting texture and of the grain size. The cold rolling texture of the austenite was simulated by means of a Taylor type model considering grain interaction and the so-called card glide mechanism. The martensite texture was characterized by  $\{211\}\langle 011 \rangle$  and  $\{111\}\langle 211 \rangle$ . The former component was interpreted in terms of the relaxation of shear constraints. The latter was attributed to selective phase transformation of  $\{011\}\langle 211 \rangle$  (austenite) to  $\{332\}\langle 113 \rangle$  (martensite) which then rotated towards  $\{111\}\langle 112 \rangle$ . The rolling textures of the martensite were simulated using a Sachs type deformation model. Copyright © 1997 Acta Metallurgica Inc.

## 1. INTRODUCTION

Stainless steel sheets are industrially manufactured by continuous casting, hot rolling, cold rolling and recrystallization. However, recent progress in producing steel sheets in pilot-scale strip casters has increasingly stimulated efforts to convert such devices to commercial production [1–6]. Unequal-diameter twin roll strip casters for the production of steels combine the two operations of casting liquid metal between two rolls and imposing a slight deformation on the solidified metal films in the rolling gap to produce coilable strips [1–4]. Strip casting provides five main improvements in comparison to conventional processing methods. First, it supplies a steel band with the same geometry as produced by hot rolling [1, 2]. This permits the hot rolling process to be bypassed. Second, the weak texture of the cast strip leads to reduced anisotropy when compared to hot rolled sheets [3, 4, 7–10]. Third, the high solidification rate leads to a refined microstructure when compared to conventional casting [11, 12]. Fourth, it is possible to directly cast steel sheets that

are not endowed with a sufficient intrinsic ductility for rolling, such as transformer steels with a high Si content [13, 14]. Fifth, it is not economical to produce small quantities of highly alloyed stainless steels by continuous casting and hot rolling.

Whilst many initial technical problems of twin roll strip casters have been solved [1, 2, 5, 6, 13, 14], the microstructure and texture that develop during rolling and annealing of strip cast austenitic steels have not yet been studied. From previous investigations on conventionally manufactured ferritic [10, 15–18] and austenitic [9, 10, 19–24] stainless steels it is known that the initial grain morphology and texture can substantially influence the texture evolution during cold rolling and annealing†.

Besides the description of the texture and microstructure that result from strip casting and subsequent processing, a second more fundamental point is of relevance as well. Unstable austenitic stainless steels undergo a strain induced phase transformation during cold rolling. This mechanism is strictly crystallographic and thus advocates the use of quantitative texture analysis. Unstable austenitic steels can thus be regarded as a model substance for studying the deformation behaviour of an f.c.c.–b.c.c. dual phase alloy.

†The recrystallization textures of the present material will be investigated in a subsequent paper [25].

Table 1. Chemical composition of austenitic stainless steel (mass %)

C	Si	Mn	Cr	Mo	Ni	Fe
0.05	0.76	1.37	18.10	0.24	8.54	Balance

Texture studies are more complicated on unstable austenitic steels than on stable ones. First, the unstable steels undergo partial strain induced phase transformation from austenite to martensite during cold rolling. Second, the transformed volume fraction of martensite depends on the deformation path. This fact represents an essential dissimilarity between the present material and 60/40 brass which is often used as a dual phase model substance [26, 27]. Third, in unstable austenites the f.c.c. and b.c.c. phases are not only coupled through stress equilibrium and strain compatibility but additionally through strict crystallographic transformation rules. Fourth, due to the nearly identical chemical composition of both phases, the {111} Bragg angle of the austenite overlaps the {110} Bragg angle of the martensite.

This paper addresses the microstructure and crystallographic texture of a strip case and subsequently cold rolled steel with 18 mass% Cr and 8.5 mass% Ni, in relation to the aforementioned points. The results are compared to those of conventionally produced samples. For this purpose identical experiments were carried out using both strip cast and hot rolled starting specimens. The microstructure and texture were studied in various through-thickness layers. The experimentally observed cold rolling textures of the austenite were compared to Taylor simulations considering grain interaction [28]. This approach was already successfully used for describing rolling textures of aluminium [29, 30]. In the present simulations both <110> and net <211> slip vectors are considered (card glide mechanism) [31, 32]. The texture of the martensite was simulated using a Sachs type deformation model considering {110}<111> and {211}<111> slip systems.

2. EXPERIMENTAL PROCEDURE

2.1. Hot rolling, strip casting and cold rolling

The chemical analysis of the specimens is given in Table 1. The samples were prepared from industrially processed hot band and from strip cast material. Hot rolling was carried out after continuous casting, slab reheating and initial reversing hot rolling in a hot strip mill, where the band was deformed in seven subsequent passes to a thickness of 2.2 mm. The temperature was between 1420 K and 1470 K during the first rolling pass and between 1050 K and 1200 K

during the last one. The strip cast specimen was produced on a pilot-scale unequal-diameter twin roll caster [1–4]. In this machine liquid steel was cast into a preheated tundish which contacted two rotating water cooled steel rolls. The steel solidified as a thin film on both roll surfaces just before reaching the bite of the rolls. The process was conducted in such a way that the contact length between the liquid metal and the roll surface was equal for both rolls. In the roll gap the films impinged and were hot compressed, receiving a thickness reduction of about 15%. The strip left the gap with a temperature of about 1370 K and a thickness of 2.4 mm [1, 2]. Both the hot rolled and the strip cast specimens were annealed at 1370 K for 20 min and subsequently descaled. Cold rolling was carried out to 80% thickness reduction ( $\Delta d/d_0$ ) in a reversing manner.

2.2. Texture measurement and calculation

The texture and microstructure of stainless steels is often inhomogeneous through the sheet thickness [9, 10, 15–19, 22]. This does not only apply to hot rolled samples but also to cold rolled samples which inherit this inhomogeneity. For this reason the texture was inspected in different thickness layers. Accordingly, in the cold rolled samples the martensitic volume fraction was metallographically determined in various layers by a selective etching technique using optical and scanning electron microscopy (SEM). For this purpose either concentrated HCl (330 K) or a solution of 50 ml H<sub>2</sub>O, 50 ml alcohol, 50 ml HCl and 2 g CuSO<sub>4</sub> was used depending on the preceding degree of deformation. For indicating the inspected layer the parameter  $s = a/(1/2d)$  was defined, where  $a$  is the distance of the investigated layer from the centre layer and  $d$  the sheet thickness.

The textures were examined by measuring the pole figures {111}, {200}, {220} and {113} of the austenitic phase and {110}, {200}, {211} and {103} of the martensitic phase using MoK $\alpha$  radiation [33]. Due to the similar chemical composition of both phases, the {111} Bragg angle of the austenite overlapped the {110} Bragg angle of the martensite. The volume fraction of martensite was determined on samples of the cold rolled hot band specimens. During rolling it gradually increased from 22 vol.% after 20% reduction up to 52 vol.% after 80% reduction (Table 2). In order to avoid ambiguities arising from the overlap, both the {110} pole figures of the martensite and the {111} pole figures of the austenite were ignored for computing the respective orientation distribution functions (ODF). The textures, which were obtained by using only non-overlapping pole

Table 2. Volume fraction of martensite in centre layer (volume %) of cold rolled hot band sample (thickness reduction,  $\Delta d/d_0$ , in %)

20%	30%	40%	50%	60%	70%	80%
22 vol. %	28 vol. %	31 vol. %	38 vol. %	43 vol. %	50 vol. %	52 vol. %

figures, were confirmed by using corrected overlapping pole figures. For this purpose the ODFs of the martensite were computed using the non-overlapping  $\{200\}$ ,  $\{211\}$  and  $\{103\}$  pole figures. Subsequently, the  $\{110\}$  projection was recalculated and subtracted from the experimental  $\{111\}_{\text{f.c.c.}} + \{110\}_{\text{b.c.c.}}$  pole figure. The subtraction was weighted by the metallographically determined volume fraction of the martensite (Table 2). After correction and normalization, the ODFs of the austenitic phase were finally calculated. The results were identical to the ODFs which were computed from the three non-overlapping pole figures. This analysis gave an idea of possible errors (up to 18% in case of the Goss component) in former texture studies on austenitic stainless steels where the textures were derived from overlapping pole figures.

From the non-overlapping pole figures the ODF was reproduced by using the iterative series expansion method ( $l_{\text{max}} = 22$ ) [34–36]. This type of pole figure inversion accounts for the non-negativity condition and for the so-called phone concept [36]. The first ingredient added to the conventional Fourier inversion methods [37], referred to as the non-negativity condition, means that negative pole densities are physically meaning. The second condition included, referred to as the phone concept [36], increases the non-negativity constraint in such a way that the minimum pole density should at least be equal not only to zero but to the pole density of an isotropic texture component (phone). This means that whilst in the conventional iterative series expansion method negative pole densities were set to zero, in the version employed here [36] they are set equal to the phone. A survey about the reliability of this method, especially with respect to a reduced number of experimental pole figures, was published by Bunge and Esling [34], Dahms and Bunge [35], Dahms [36] and Raabe [38].

In the case of cubic crystal symmetry, an orientation can be represented by the Euler angles  $\varphi_1$ ,  $\phi$  and  $\varphi_2$ . For orthorhombic sample symmetry which is set up by the rolling (RD), normal (ND) and transverse (TD) directions, the Euler angles range from 0 to  $\pi/2$ . However, if strong shear strains prevail, the sample symmetry is no longer orthorhombic but monoclinic, which requires that one of the Euler angles ranges from 0 to  $\pi$ . Although the latter case is encountered with hot rolled materials, the corresponding textures are presented by using the reduced angles ( $0-\pi/2$ ). The artificial symmetrization that arises from this simplification is negligible. An orientation can also be described in terms of the Miller indices  $\{hkl\}\langle uvw \rangle$ , where  $\{hkl\}$  indicates the crystal plane parallel to the sheet surface and  $\langle uvw \rangle$  the direction parallel to RD. Since both the austenite and the martensite tend to develop characteristic fibre textures during rolling and annealing, it is convenient to present the data in the form of ODF sections or fibre diagrams. Relevant fibres for austenite textures are the  $\alpha_{\text{fcc}}$ -fibre ( $\langle 011 \rangle$  parallel to the ND), the  $\tau$ -fibre ( $\langle 110 \rangle$  parallel to the TD), the  $\beta$ -fibre (less symmetric fibre comprising  $\{211\}\langle 111 \rangle$ ,  $\sim \{123\}\langle 634 \rangle$  and  $\{011\}\langle 211 \rangle$ ) and the cube fibres showing rotations of  $\{001\}\langle 100 \rangle$  about RD, TD and ND. The  $\beta$ -fibre is a so-called skeleton line, i.e. its position may vary according to the local texture maximum. Its presentation thus requires two plots showing the orientation density of the  $\beta$ -fibre components and their coordinates in Euler space. For presenting martensite textures, the  $\alpha_{\text{bcc}}$ -fibre ( $\langle 011 \rangle$  parallel to the RD) and the  $\tau$ -fibre ( $\langle 110 \rangle$  parallel to the TD) were employed. Some frequent texture components are indicated by names, such as the 'Brass' or 'B' ( $\{011\}\langle 211 \rangle$ ), the 'Copper' or 'C' ( $\{211\}\langle 111 \rangle$ ), the 'S' ( $\sim \{123\}\langle 634 \rangle$ ), the 'Goss' ( $\{011\}\langle 100 \rangle$ ), and the 'Cube' component ( $\{001\}\langle 100 \rangle$ ).

Fig. 1. Microstructure of hot rolled austenitic stainless steel. (a,b) Flat sections close to surface layer; (c) flat section in centre layer showing some martensite platelets.

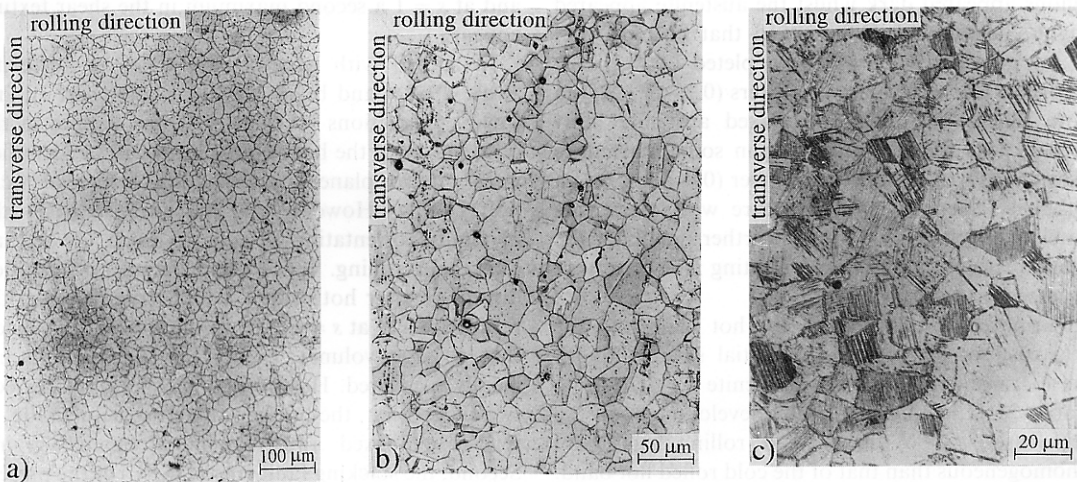


Fig. 1. Microstructure of hot rolled austenitic stainless steel. (a,b) Flat sections close to surface layer; (c) flat section in centre layer showing some martensite platelets.

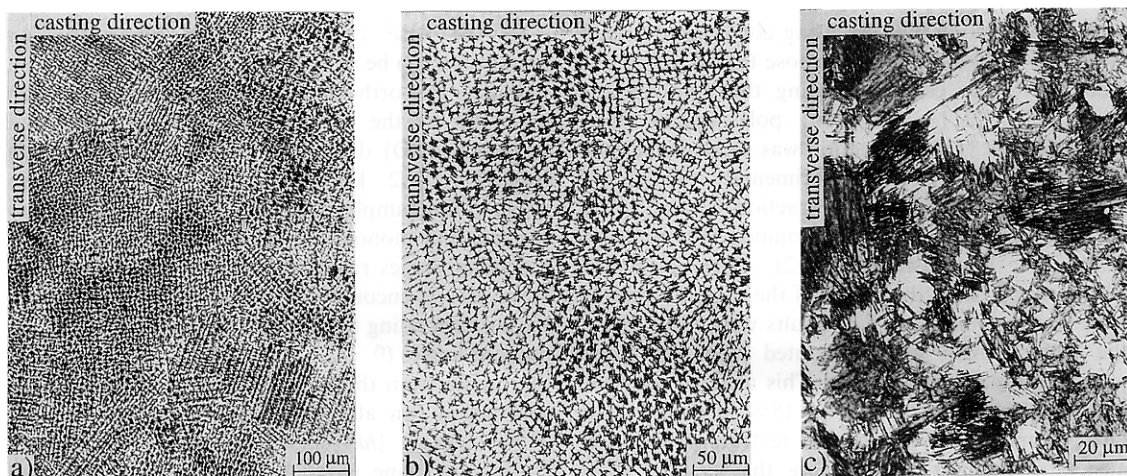


Fig. 2. Microstructure of strip cast austenitic stainless steel. (a,b) Flat sections showing blocks of austenitic dendrites (bright) with microsegregated interdendritic regions (dark) close to surface layer; (c) flat section in centre layer showing a globular austenitic grain structure with martensite platelets.

### 3. RESULTS AND DISCUSSION

#### 3.1. Microstructure

Figures 1 and 2 show the microstructure of the starting material. The hot band had a homogeneous microstructure with an average grains size of  $35\ \mu\text{m}$ . Close to the surface layers [Figs 1(a),(b)] many twin boundaries but no martensite occurred. In the centre layers both coherent and incoherent twin boundaries, strain induced martensite and a small volume fraction of retained  $\delta$ -ferrite was found [Fig. 1(c)]. The strip case austenite (Fig. 2) revealed a less homogeneous microstructure when compared to the hot band. Between the surface and the near-centre layers ( $0.4 \leq s \leq 1.0$ ) cylindrical, uniformly oriented blocks of austenitic primary dendrites which were branched out up to the second generation were observed [Figs 2(a),(b)]. These blocks had an average diameter of  $140\ \mu\text{m}$  and a length of up to  $500\ \mu\text{m}$  parallel to the growth direction. In the flat sections [Figs 2(a),(b)] the microsegregated interdendritic regions appeared dark whilst the austenite appeared bright. Siegel *et al.* [39] showed that both Ni and Cr are enriched whilst Fe is depleted between the dendrites. Close to the centre layers ( $0.1 \leq s \leq 0.3$ ) a more blocky and nearly equiaxed austenite morphology was found. In this region some martensite occurred as well. In the centre layer ( $0.0 \leq s \leq 0.1$ ) a globular austenitic grain structure with martensite platelets appeared [Fig. 2(c)]. Further details of the initial microstructure of both starting materials were discussed elsewhere [9, 19].

During cold rolling, both the hot band and the strip cast sample revealed a partial strain induced phase transformation from austenite to martensite (Table 2). The microstructure development of the strip case sample during cold rolling was more inhomogeneous than that of the cold rolled hot band. The rolled strip case sample revealed dendritic austenite grains, martensite and the microsegregated

interdendritic regions which penetrated the matrix with a skeleton type topology.

#### 3.2. Crystallographic textures

**3.2.1. Hot rolling.** Figure 3 shows the thickness profile of the hot band texture. Close to the centre layer ( $0.0 \leq s \leq 0.1$ ) the texture is dominated by an incomplete  $\alpha_{\text{f.c.c.}}$ -fibre with a pronounced B, C and cube component. At  $s = 0.2$  a nearly random texture is revealed. In the intermediate layers ( $0.5 \leq s \leq 0.6$ ) a weak  $\{001\}\langle 110 \rangle$  [Fig. 3(b)], a  $\{111\}\langle 211 \rangle$  [Fig. 3(b)] and a  $\{211\}\langle 110 \rangle$  orientation are observed. In the sub-surface layers ( $0.7 \leq s \leq 0.8$ ) the texture is again nearly randomized. At the surface ( $s = 1.0$ ), a similar texture as in layer  $s = 0.6$  is developed. Figure 4 shows the profile of the main shear texture components through the thickness of the hot band. Close to the centre layers the shear components are weak and increase in intensity up to  $s = 0.6$ . Between  $s = 0.6$  and  $s = 0.9$  a degradation and at  $s = 1$  a second maximum in the shear texture appear.

In accord with experimental data on austenitic steels [19–24] and brass [e.g. 26, 27, 40 (part I)] and Taylor predictions [40 (part II)], the texture in the centre layer of the hot band (Fig. 3) can be identified as a typical plane strain rolling texture of f.c.c. polycrystals. However, in the present case, the maximum orientation density is much lower than after cold rolling. Since complete recrystallization during or after hot rolling would have removed the rolling texture at  $s = 0$ , this result appears to suggest that a large volume fraction of the material has merely recovered. However, this conclusion neglects two facts. First, the hot band microstructure (Fig. 1) reveals equiaxed rather than elongated grains. Second, the stacking fault energy (SFE) of the present alloys is low ( $21 \times 10^{-3}\ \text{J/m}^2$ ) [41]. The normalized value, i.e. the SFE divided by the Burgers vector and

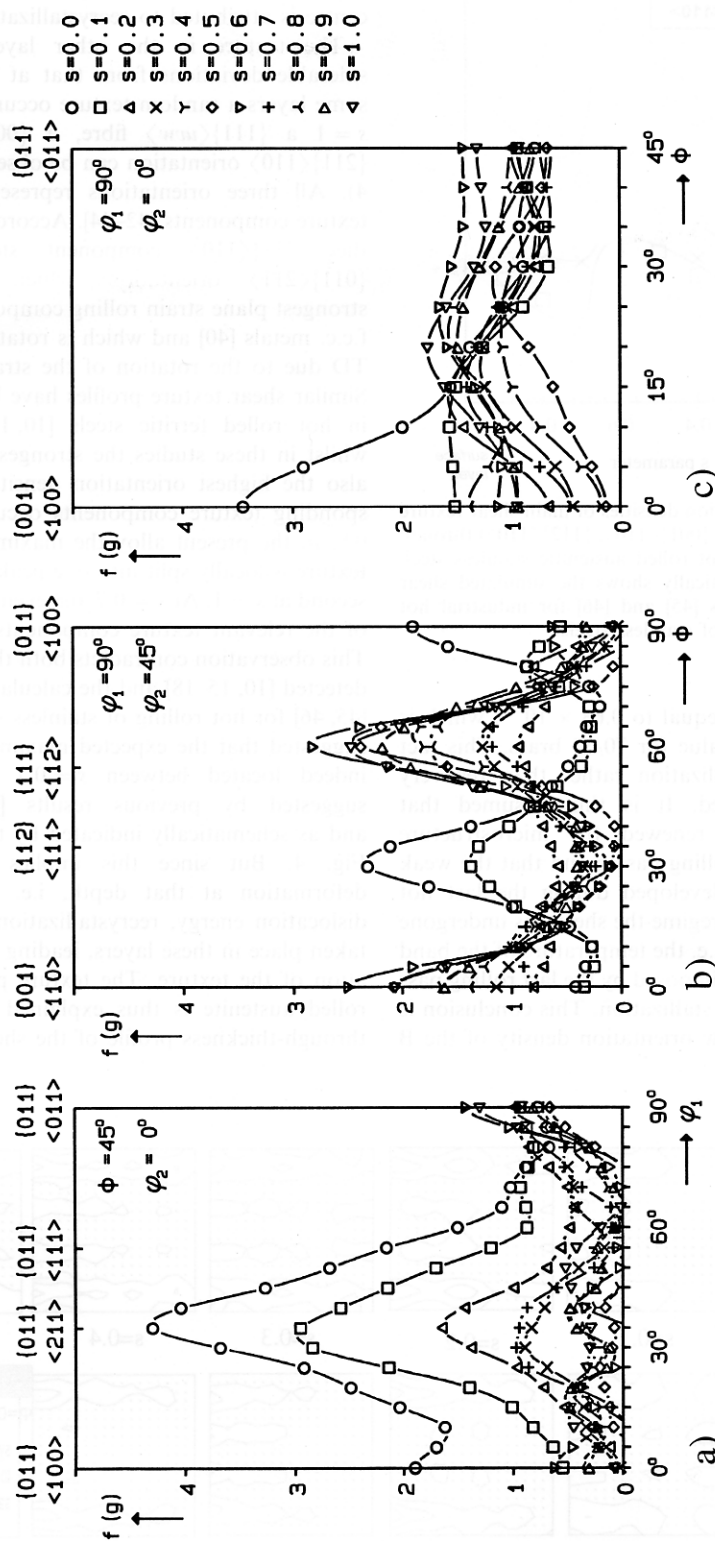


Fig. 3. Experimental texture of hot rolled austenitic stainless steel, for various through-thickness layers. (a)  $\alpha_{fcc}$ -fibre, (b)  $\tau$ -fibre, (c) cube fibre comprising rotations of cube component about transverse direction.

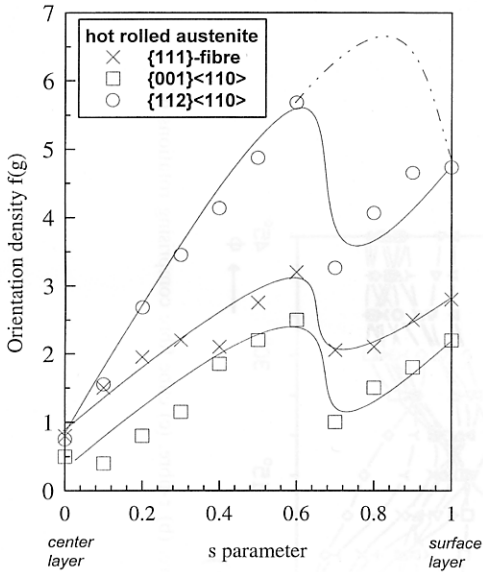


Fig. 4. Profile of orientation densities of main shear texture components ( $\{111\}$  fibre,  $\{001\}\langle 110 \rangle$ ,  $\{112\}\langle 110 \rangle$ ) through the sheet thickness of hot rolled austenitic stainless steel. The dotted line schematically shows the simulated shear strain according to Refs [45] and [46] for industrial hot rolling of stainless steels.

the shear modulus is equal to  $0.68 \times 10^{-3}$ , which is of the order of the value for 70/30 brass. This fact implies that recrystallization rather than recovery should have prevailed. It is thus assumed that recrystallization has renewed the microstructure during the first hot rolling passes and that the weak rolling texture was developed during the last hot rolling passes. In this regime the sheet has undergone considerable cooling, i.e. the temperature of the band and the stored energy imposed by the last rolling pass were too low for recrystallization. This conclusion is in accord with the low orientation density of the B

component [ $f(g) = 4.3$ ] since recovery of rolled material would have led to a much stronger texture maximum. The cube component in the hot band centre is attributed to recrystallization.

The texture in the other layers reveals considerable deviations from that at  $s = 0$ . Whilst in some layers a random texture occurs, at  $s = 0.6$  and  $s = 1$  a  $\{111\}\langle uvw \rangle$  fibre, a  $\{001\}\langle 110 \rangle$  and a  $\{211\}\langle 110 \rangle$  orientation can be observed (Figs 3 and 4). All three orientations represent typical shear texture components [42–44]. According to Mao [44], the  $\{211\}\langle 110 \rangle$  component stems from the  $\{011\}\langle 211 \rangle$  orientation, which represents the strongest plane strain rolling component in low SFE f.c.c. metals [40] and which is rotated  $30^\circ$  about the TD due to the rotation of the strain state [43, 44]. Similar shear texture profiles have been investigated in hot rolled ferritic steels [10, 15–18]. However, whilst in these studies the strongest shear and thus also the highest orientation densities of the corresponding texture components occurred at  $s = 0.7–0.8$ , in the present alloy the maximum of the shear texture is locally split into one peak at  $s = 0.6$  and a second at  $s = 1$ . At  $s = 0.7–0.8$  even a local minimum of the relevant texture components occurs (Fig. 4). This observation contradicts both the experimentally detected [10, 15–18] and the calculated shear profiles [45, 46] for hot rolling of stainless steels. Hence it is suggested that the expected maximum of shear was indeed located between  $s = 0.7$  and  $s = 0.8$ , as suggested by previous results [10, 15–18, 45, 46] and as schematically indicated by the dotted line in Fig. 4. But since this implies a higher local deformation at that depth, i.e. a higher stored dislocation energy, recrystallization can easily have taken place in these layers, leading to the randomization of the texture. The texture profile of the hot rolled austenite is thus explained in terms of the through-thickness profile of the shear strain.

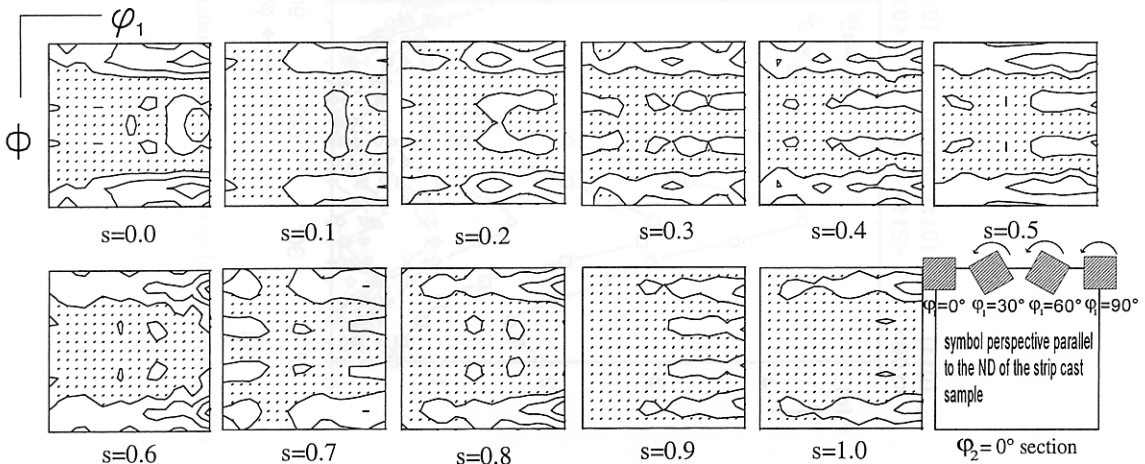


Fig. 5. Experimental texture of strip cast austenitic stainless steel, weak texture fibre close to  $\{001\}\langle uvw \rangle$ , various through-thickness layers ( $s = 0$ : centre layer,  $s = 1$ : surface layer),  $\phi_2 = 0^\circ$  sections,  $0 \leq \phi_1 \leq \pi/2$ ,  $0 \leq \phi \leq \pi/2$ , iso-lines at  $f(g) = 1, 1.5, 2, 2.5, 3$ .



3.2.2. *Strip casting.* The texture of the strip cast material is weak and does not show relevant texture gradients. In all layers a weak  $\{001\}\langle uwv \rangle$  texture fibre occurs (Fig. 5). The micrographs show that the

surface layers consist of undeformed large blocks of austenitic dendrites (Fig. 2). The observed texture fibre is thus attributed to growth selection. From directional solidification experiments on Al it is well

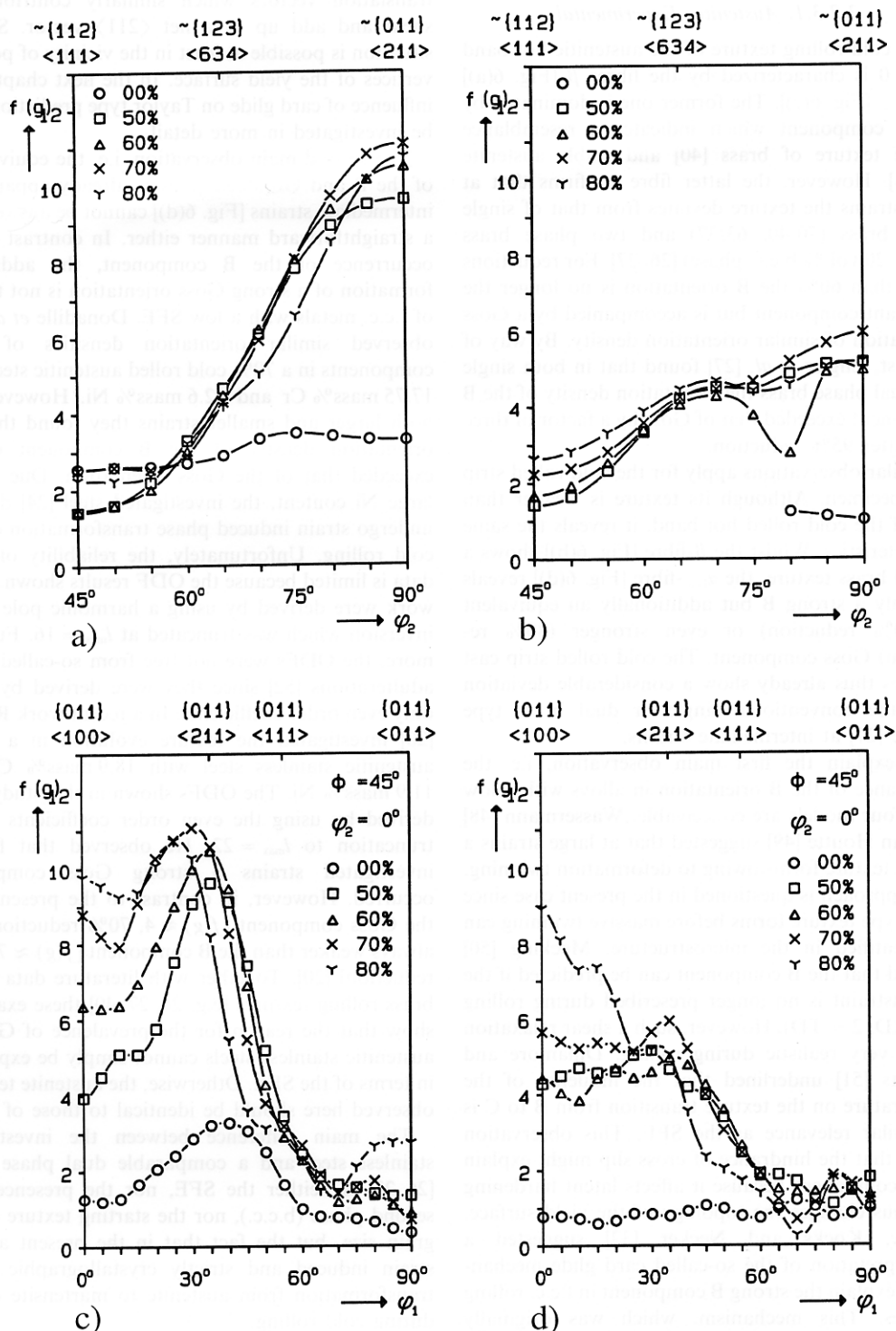


Fig. 6. Experimental cold rolling texture of hot band and strip cast austenite in centre layer. (a)  $\beta$ -fibre, cold rolled (hot band starting sample), (b)  $\beta$ -fibre, cold rolled (strip cast starting sample), (c)  $\alpha_{fcc}$ -fibre, cold rolled (hot band starting sample), (d)  $\alpha_{fcc}$ -fibre, cold rolled (strip cast starting sample).

established that  $\{100\}\langle u\bar{v}w \rangle$  has a larger growth rate than other orientations [47]. Further details of the strip casting textures were discussed elsewhere [9, 10].

### 3.2.3. Cold rolling.

#### 3.2.3.1. Austenite, Experimental

The cold rolling texture of the austenitic hot band at  $s = 0$  is characterized by the fibres  $\beta$  [Fig. 6(a)] and  $\alpha_{f.c.c.}$  [Fig. 6(c)]. The former one is dominated by the B component which indicates a resemblance to the texture of brass [40] and stable austenite [20, 24]. However, the latter fibre confirms that at large strains the texture deviates from that of single phase brass (70/40, 63/37) and two phase brass (60/40, 20 vol.% b.c.c. phase) [26, 27]. For reductions larger than 60% the B orientation is no longer the dominant component but is accompanied by a Goss orientation of similar orientation density. By way of contrast, Engler *et al.* [27] found that in both single and dual phase brass the orientation density of the B component exceeded that of Goss by a factor of three even after 95% reduction.

Similar observations apply for the cold rolled strip cast specimen. Although its texture is weaker than that of the cold rolled hot band, it reveals the same characteristics. Whilst the  $\beta$ -fibre [Fig. 6(b)] shows a typical brass texture, the  $\alpha_{f.c.c.}$ -fibre [Fig. 6(d)] reveals not only a strong B but additionally an equivalent (50–70% reduction) or even stronger (80% reduction) Goss component. The cold rolled strip cast samples thus already show a considerable deviation from the conventional single or dual brass type texture [27] at intermediate strains.

To explain the first main observation, i.e. the dominance of the B orientation in alloys with a low SFE, four models are conceivable. Wassermann [48] and van Houtte [49] suggested that at large strains a B type texture forms owing to deformation twinning. This approach is questioned in the present case since the B type texture forms before massive twinning can be identified in the microstructure. Mecking [50] showed that the B component can be predicted if the  $e_{12}$  constraint is no longer prescribed during rolling ( $1 = \text{RD}$ ,  $2 = \text{TD}$ ). However, such a shear relaxation is not very realistic during rolling. Dillamore and Roberts [51] underlined that the influence of the temperature on the texture transition from B to C is of similar relevance as the SFE. This observation shows that the hindrance of cross slip might explain the B component because it affects latent hardening and thus changes the topology of the yield surface. Finally, Kocks and Necker [32] suggested a reinterpretation of the so-called card glide mechanism to explain the strong B component in f.c.c. rolling textures. This mechanism, which was originally suggested by Hu *et al.* [31], is based on a fixed  $\{111\}$  glide plane in which slip can operate with arbitrary Burgers vectors. Both the conventional  $\langle 110 \rangle$  and the partial  $\langle 211 \rangle$  glide vectors are conceivable. However,

plastic flow by activation of single  $\langle 211 \rangle$  Shockley type slip vectors is not likely since it would lead to excessive faulting. However, Kocks and Necker [32] pointed out that net  $\langle 211 \rangle$  slip can also be achieved by simultaneous glide using two conventional  $\langle 110 \rangle$  translation vectors which similarly contribute to shear and add up to a net  $\langle 211 \rangle$  vector. Such a situation is possible at least in the vicinity of polyslip vertices of the yield surface. In the next chapter the influence of card glide on Taylor type predictions will be investigated in more detail.

The second main observation, i.e. the equivalence of the B and Goss orientations already apparent at intermediate strains [Fig. 6(d)] cannot be answered in a straightforward manner either. In contrast to the occurrence of the B component, the additional formation of a strong Goss orientation is not typical of f.c.c. metals with a low SFE. Donadille *et al.* [24] observed similar orientation densities of both components in a 70% cold rolled austenitic steel with 17.75 mass% Cr and 12.6 mass% Ni. However, for both larger and smaller strains they found that the orientation density of the B component clearly exceeded that of the Goss orientation. Due to the large Ni content, the investigated steel [24] did not undergo strain induced phase transformation during cold rolling. Unfortunately, the reliability of these data is limited because the ODF results shown in this work were derived by using a harmonic pole figure inversion which was truncated at  $l_{\max} = 16$ . Furthermore, the ODFs were not free from so-called ghost adulterations [52] since they were derived by using only even order coefficients. In a recent work Rickert [20] investigated the texture evolution in a stable austenitic stainless steel with 18.9 mass% Cr and 11.9 mass% Ni. The ODFs shown in this study were derived by using the even order coefficients and a truncation to  $l_{\max} = 22$ . He observed that for all investigated strains a strong Goss component occurred. However, in contrast to the present data the Goss component [ $f(g) \approx 4$ , 70% reduction] was always weaker than the B component [ $f(g) \approx 7$ , 70% reduction] [20]. Together with literature data about brass rolling textures [e.g. 26, 27, 40] these examples show that the reason for the prevalence of Goss in austenitic stainless steels cannot simply be explained in terms of the SFE. Otherwise, the austenite textures observed here should be identical to those of brass.

The main difference between the investigated stainless steel and a comparable dual phase brass [26, 27] is neither the SFE, nor the presence of a second phase (b.c.c.), nor the starting texture or the grain size, but the fact that in the present alloy a strain induced and strictly crystallographic phase transformation from austenite to martensite occurs during cold rolling.

In a thorough study Goodchild *et al.* [53] have investigated the martensitic phase transformation at various temperatures in two polycrystalline, textured, austenitic stainless steels with 17.36 mass% Cr,



7.2 mass% Ni and 17.36 mass% Cr, 7.2 mass% Ni, respectively. They observed that after tensile deformation in the unstable temperature region, martensite was formed in all grains except in those extended along  $\langle 001 \rangle$ . Conversely, compressive deformation caused transformation in grains compressed along  $\langle 001 \rangle$  but not in grains in which the compression axis was close to  $\langle 011 \rangle$ . This observation is of considerable relevance to the interpretation of the present textures. In a simple approach the externally imposed stress deviator may be decomposed into a compression component parallel to the ND and a tensile component parallel to the RD [54]. Consequently, any orientation which has a crystal  $\langle 011 \rangle$  direction parallel to the compression axis (ND) and a  $\langle 100 \rangle$  direction parallel to the tensile axis (RD) will be stable with respect to strain induced phase transformation. This criterion is indeed fulfilled by the Goss component,  $\{011\}\langle 100 \rangle$ . The B orientation,  $\{011\}\langle 211 \rangle$ , likewise reveals a  $\langle 011 \rangle$  direction parallel to the ND, but no  $\langle 100 \rangle$  direction parallel to the RD. It is thus conceivable that the B orientation is less stable with respect to martensitic phase transformation than the Goss component. In analogy to the phenomenon of variant selection, where particular martensite variants prevail due to external or internal constraints, the present phenomenon will hereafter be referred to as selective transformation.

If the B component indeed undergoes selective martensitic phase transformation during cold rolling it should lead to two characteristic texture changes. First, one would expect a degradation or at least a stagnation of its orientation density in the f.c.c. texture. Second, its transformation should entail a new texture component in the martensite with a strict crystallographic relationship to the B component. The first conclusion is indeed covered by the textures shown in Fig. 6. In the strip cast and in the hot rolled material the orientation density of the B component clearly stagnates at intermediate and large strains. The second prediction will be investigated in Section 3.2.3.3 by analysing the texture of the martensite.

The fact that the cold rolling texture of the strip cast alloy is generally weaker than that of the hot band is attributed to the grain size and to the starting texture. Samples with a large grain size often reveal low crystal rotation rates and grain fragmentation which altogether weaken the texture. Furthermore, the starting texture of the hot band sample already contained a weak  $\beta$ -fibre prior to cold rolling.

### 3.2.3.2. Austenite, Simulation

Following the approach of Hu *et al.* [31] in the reinterpretation of Kocks and Necker [32], the cold rolling textures of the austenite were simulated by means of a modified Taylor model which considers grain interaction and both  $\langle 110 \rangle$  and net  $\langle 211 \rangle$  slip vectors in the  $\{111\}$  glide planes (card glide mechanism). According to Kocks and Necker [32] the

net  $\langle 211 \rangle$  slip vectors are not interpreted as partial slip vectors but as simultaneously contributing  $\langle 110 \rangle$  vectors which add up to a net  $\langle 211 \rangle$  vector.

For simulating deformation textures, two Taylor type approaches were mainly used in the past. In the "Full Constraints" models (FC) [55] the external strain tensor is prescribed for each grain where it has to be accomplished by slip. In the "Relaxed Constraints" models (RC) [56–58] some external shear components need not be fulfilled. This assumption leads to a reduction in the number of active slip systems and hence to a lower Taylor energy as compared to the FC model. In a new Taylor approach by Schmitter and Lücke [28] the shears are only partially relaxed according to the gain in deformation energy which depends on the orientation. The shear dependent degradation of the Taylor energy is quantified by the shear capacity, which is defined as the maximum slope of the plane which combines the deformation energy predicted by the FC model with that computed by the RC model [28]. The shear capacity thus depends on the grain orientation and is a measure of the gain in energy that is achieved if a particular shear component is relaxed.

For simulating cold rolling of austenite,  $\{111\}\langle 110 \rangle$  and net  $\{111\}\langle 211 \rangle$  slip systems were used [31, 32]. The ratio between the critical resolved shear stress (CRSS) for slip in the net  $\langle 211 \rangle$  and  $\langle 110 \rangle$  directions,  $\alpha = \tau^{\langle 211 \rangle} / \tau^{\langle 111 \rangle}$ , was varied between  $2/\sqrt{3}$  and 0.96 [32]. In all simulations an ideal plane strain state was prescribed. The rolling textures were computed up to 80% thickness reduction, starting from a random texture consisting of 936 orientations. The ODFs were calculated by using Gauss functions with a scatter width of  $11^\circ$ .

Figure 7 shows the  $\beta$ -fibre and the  $\alpha_{f.c.c.}$ -fibre for  $\alpha = 2/\sqrt{3}$  [32]. In particular, the strong dominance of the C component on the  $\beta$ -fibre does not reflect the experimental results (Fig. 6). The same applies for  $\alpha = 1$  and  $\alpha = 0.98$ . Although for these values the B component reveals a similar orientation density to the C component, the experimentally observed dominance of the B orientation is not covered. However, if the CRSS ratio is decreased to  $\alpha = 0.96$  (Fig. 8), the predictions yield good agreement with the experimental results (Fig. 6). Provided that the card glide mechanism has a physical basis at least for orientations in the vicinity of polyslip vertices of the yield surface, it is concluded that the corresponding CRSS ratio has a value slightly below unity.

It is worth emphasizing that both the experimental and simulated ( $\alpha = 0.96$ ) data are very similar to  $90^\circ$  about the TD rotated textures of b.c.c. materials. In a former study [43] which focused on the similarity of f.c.c. and b.c.c. rolling textures it was shown that an identity of both texture types only results under particular strain constraints. Further deviations, which became apparent especially on the respective  $\alpha$ -fibres, were attributed to the fact that rather than only one, in b.c.c. two or even three types of slip

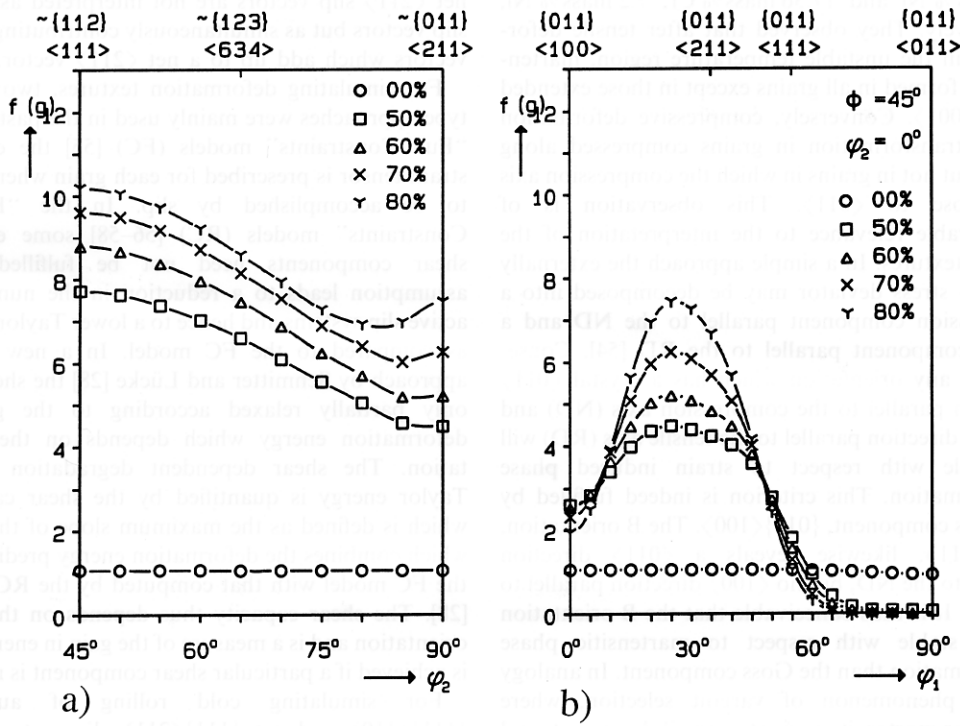


Fig. 7. Simulation of cold rolling textures of austenite by means of a modified RC Taylor model which considers grain interaction [29] and both  $\langle 110 \rangle$  and net  $\langle 211 \rangle$  slip vectors on  $\{111\}$  glide planes (card glide mechanism). Following the approach of Hu *et al.* [31] in the reinterpretation of Kocks and Necker [32] the  $\langle 211 \rangle$  slip vectors are interpreted as equally contributing  $\langle 110 \rangle$  type vectors which add up to a net  $\langle 211 \rangle$  vector. The CRSS ratio between  $\langle 211 \rangle$  and  $\langle 110 \rangle$  slip was  $\alpha = \tau^{(211)} / \tau^{(111)} = 2/\sqrt{3}$ , texture smoothed by  $11^\circ$  scatter width, starting texture: 936 randomly distributed orientations. (a)  $\beta$ -fibre, (b)  $\alpha_{fcc}$ -fibre.

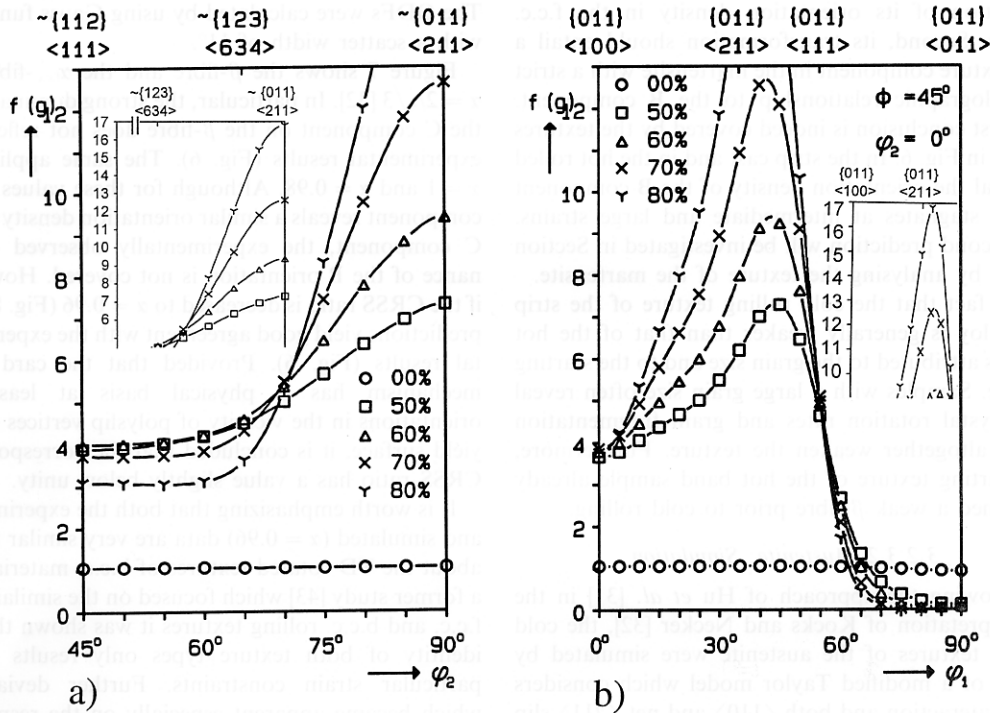


Fig. 8. Simulation of cold rolling textures of austenite, same approach as shown in Fig. 7. The CRSS ratio between  $\langle 211 \rangle$  and  $\langle 110 \rangle$  slip was  $\alpha = \tau^{(211)} / \tau^{(111)} = 0.96$ . (a)  $\beta$ -fibre, (b)  $\alpha_{fcc}$ -fibre.

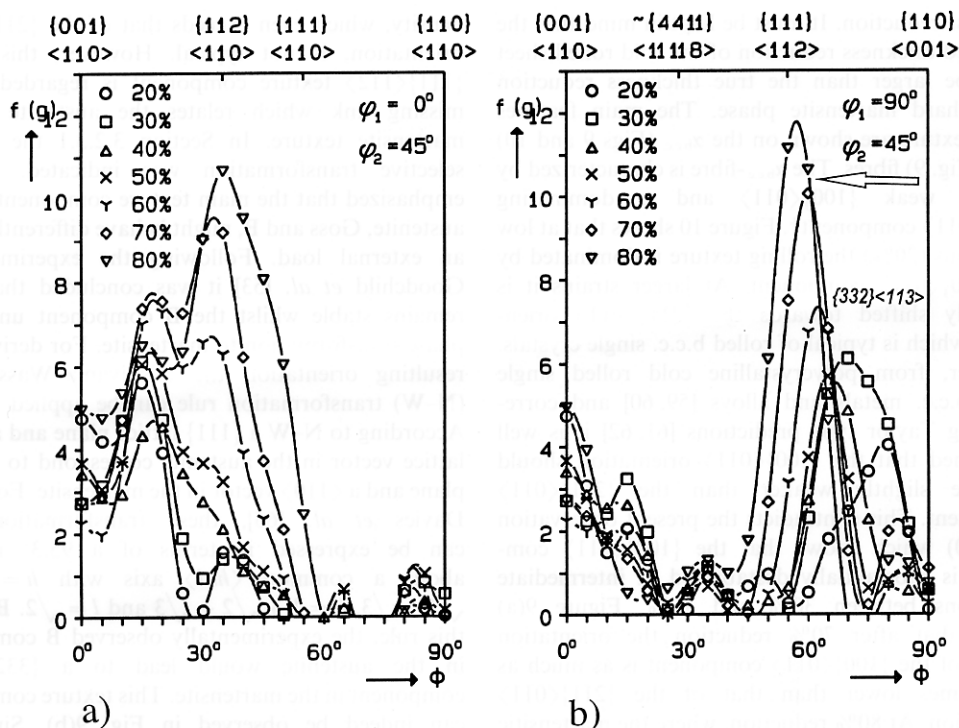


Fig. 9. Experimental cold rolling texture of strain induced martensite phase of hot band (Table 2). ODF derived from three non-overlapping pole figures. (a)  $\alpha_{b.c.c.}$ -fibre, (b)  $\tau$ -fibre.

system are typically active. This argument obviously no longer holds for f.c.c. alloys which deform via  $\{111\}\langle 110\rangle$  and net  $\{111\}\langle 211\rangle$  glide systems since they correspond to the  $90^\circ$  about the TD rotated b.c.c.  $\{110\}\langle 111\rangle$  and  $\{112\}\langle 111\rangle$  glide systems. As mentioned earlier [32], the card glide mechanism in

f.c.c. thus corresponds to the  $90^\circ$  about the TD rotated pencil glide mechanism in b.c.c.

### 3.2.3.3. Martensite, Experimental

The martensite texture generated in the cold rolled hot band was studied in detail between 20% and 80%

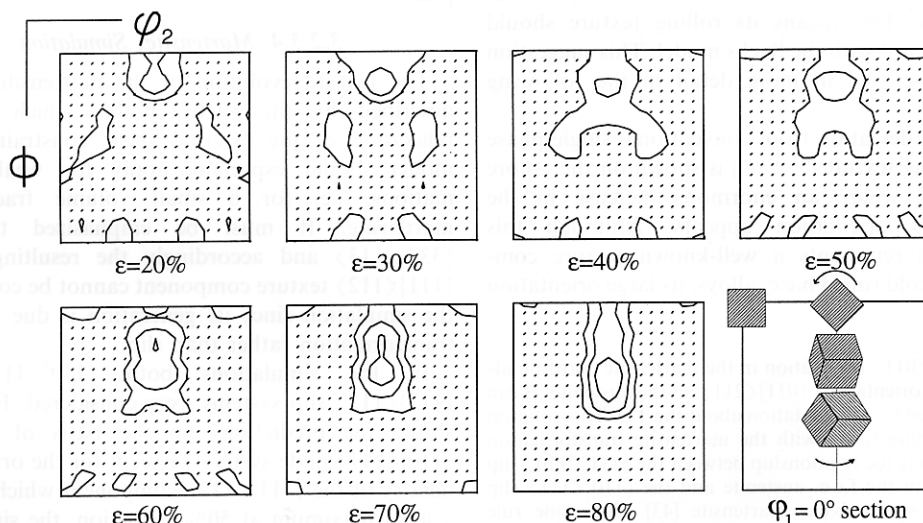


Fig. 10. Experimental cold rolling texture of strain induced martensite phase of hot band (Table 2). ODF derived from three non-overlapping pole figures,  $\phi_1 = 0^\circ$  sections,  $0 \leq \phi_2 \leq \pi/2$ ,  $0 \leq \phi \leq \pi/2$ , ( $\alpha_{b.c.c.}$ -fibre at  $\phi_2 = 45^\circ$ ), iso-lines at  $f(g) = 2, 4, 7$ .

thickness reduction. It must be kept in mind that the measured thickness reduction of the cold rolled sheet might be larger than the true thickness reduction of the hard martensite phase. The main features of the texture are shown on the  $\alpha_{\text{b.c.c.}}$  (Figs 9 and 10) and  $\tau$  (Fig. 9) fibres. The  $\alpha_{\text{b.c.c.}}$ -fibre is characterized by a very weak  $\{100\}\langle 011\rangle$  and a dominating  $\{211\}\langle 011\rangle$  component†. Figure 10 shows that at low reductions (20%) the rolling texture is dominated by the  $\{100\}\langle 011\rangle$  component. At larger strains it is gradually shifted towards the  $\{211\}\langle 011\rangle$  orientation, which is typical of rolled b.c.c. single crystals. However, from polycrystalline cold rolled single phase b.c.c. metals and alloys [59, 60] and corresponding Taylor type predictions [61, 62] it is well established that the  $\{100\}\langle 011\rangle$  orientation should only be slightly weaker than the  $\{211\}\langle 011\rangle$  component. This contradicts the present observation (Fig. 10) which shows that the  $\{100\}\langle 011\rangle$  component is substantially destabilized at intermediate reductions between 30% and 70%. Figure 9(a) reveals that after 70% reduction the orientation density of the  $\{100\}\langle 011\rangle$  component is as much as three times lower than that of the  $\{211\}\langle 011\rangle$  orientation. At 80% reduction, where the martensitic volume fraction amounts to 52 vol.% this tendency seems to stagnate, i.e. the  $\{100\}\langle 011\rangle$  component starts to increase.

In accord with previous investigations on dual phase 60/40 brass [27], the weak  $\{100\}\langle 011\rangle$  component at thickness reductions below 70% is attributed to the different plastic behaviour and to the different strain constraints that control the deformation of the martensitic phase. First, the martensite is harder than the austenite and second, except for the maximum investigated reduction (80%), the martensite represents the minority phase. Both parameters suggest that the martensite can essentially deform as a hard particle in a soft matrix, i.e. with less shear constraints. This means its rolling texture should form in accord with the Sachs model. This suggestion will be discussed in more detail in the following chapter.

Another deviation from conventional single phase b.c.c. rolling textures [59, 60] is shown on the  $\tau$ -fibre [Fig. 9(b)] where an enormous increase in the  $\{111\}\langle 211\rangle$  orientation appears. Although this orientation represents a well-known texture component in cold rolled b.c.c. alloys, its large orientation

density, which even exceeds that of the  $\{211\}\langle 110\rangle$  orientation, is not typical. However, this strong  $\{111\}\langle 112\rangle$  texture component is regarded as the missing link which relates the austenite to the martensite texture. In Section 3.2.3.1 the idea of selective transformation was indicated. It was emphasized that the main texture components in the austenite, Goss and B, might behave differently under an external load. Following the experiments of Goodchild *et al.* [53] it was concluded that Goss remains stable whilst the B component undergoes phase transformation to martensite. For deriving the resulting orientation the Nishiyama–Wassermann (N–W) transformation rule can be applied [63–67]. According to N–W a  $\{111\}$  lattice plane and a  $\langle 211\rangle$  lattice vector in the austenite correspond to a  $\{110\}$  plane and a  $\langle 110\rangle$  vector in the martensite. Following Davies *et al.* [65], these transformation rules can be expressed in terms of a  $95.3^\circ$  rotation about a common  $\langle hkl\rangle$  axis with  $h = -1 + \sqrt{2} + \sqrt{3}$ ,  $k = 1 + \sqrt{2} + \sqrt{3}$  and  $l = \sqrt{2}$ . By using this rule, the experimentally observed B component in the austenite would lead to a  $\{332\}\langle 113\rangle$  component in the martensite. This texture component can indeed be observed in Fig. 9(b). Since the  $\{332\}\langle 113\rangle$  orientation is not stable under plane strain rolling conditions it rotates towards the  $\{111\}\langle 112\rangle$  component (arrow). The present data thus strongly suggest that the mechanism of selective transformation indeed takes place during cold rolling of an unstable austenite. However, the transformation of the B component does not directly lead to the observed, strong  $\{111\}\langle 112\rangle$  orientation, but first to the neighbouring  $\{332\}\langle 113\rangle$  component which then rotates about the TD towards  $\{111\}\langle 112\rangle$ . This mechanism represents an important deviation from the behaviour of 60/40 brass since it establishes a close crystallographic relationship between the two phases.

### 3.2.3.4. Martensite, Simulation

The texture evolution of the martensite can be described by the Sachs model, which assumes relaxation of the external shear constraints. This model should especially apply for weak deformations, i.e. for a small volume fraction of martensite. It must be emphasized that the  $\{332\}\langle 113\rangle$  and accordingly the resulting strong  $\{111\}\langle 112\rangle$  texture component cannot be covered by the simulation since its generation is due to phase transformation rather than slip.

In the simulations both  $\{110\}\langle 111\rangle$  and  $\{112\}\langle 111\rangle$  slip systems were considered. Figure 11 shows the predictions on the basis of only 12  $\{110\}\langle 111\rangle$  glide systems. Except for the orientation density of the  $\{111\}\langle 112\rangle$  component which reaches a local maximum at 50% reduction, the simulation yields reasonable agreement with experiment (Fig. 9). Corresponding predictions on the basis of 12  $\{110\}\langle 111\rangle$  and 12  $\{112\}\langle 111\rangle$  glide

†The  $\{211\}\langle 011\rangle$  orientation in the martensite corresponds to the B orientation,  $\{011\}\langle 211\rangle$ , in the austenite. It can be derived by a  $90^\circ$  rotation about the TD. This rotation has nothing to do with the martensite transformation but reflects the relationship between the  $\{111\}\langle 110\rangle$  slip systems in the f.c.c. austenite and the  $\{110\}\langle 111\rangle$  slip systems in the b.c.c. martensite [43]. The same rule applies to the relationship between the  $\{011\}\langle 100\rangle$  (Goss, f.c.c.) and the  $\{001\}\langle 110\rangle$  (b.c.c.) and the  $\{112\}\langle 111\rangle$  (C, f.c.c.) and the  $\{111\}\langle 112\rangle$  (b.c.c.) orientations.

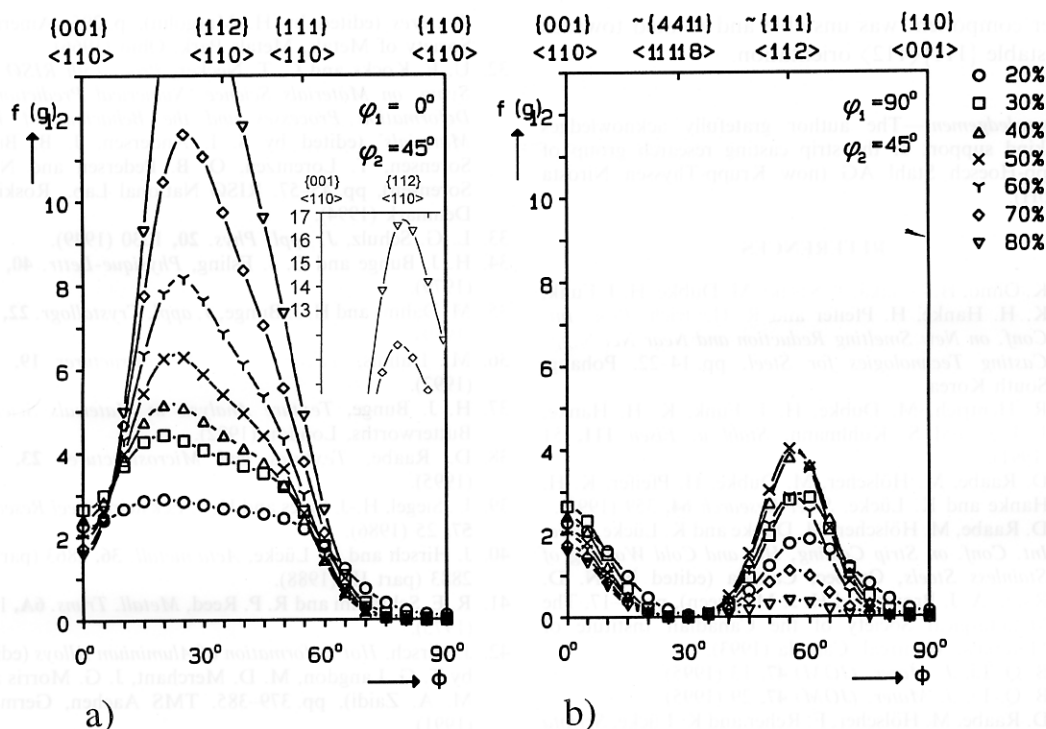


Fig. 11. Sachs type texture simulation, strain induced martensite in cold rolled hot band sample (Table 2), 20–80% thickness reduction, 12  $\{110\} \langle 111 \rangle$  glide systems, texture smoothed by  $11^\circ$  scatter widths, starting texture: 936 randomly distributed orientations. (a)  $\alpha_{\text{bcc}}$ -fibre, (b)  $\tau$ -fibre.

systems yielded less correspondence to experiment. The validity of the Sachs type approach for the description of the minor b.c.c. phase in a softer f.c.c. matrix has already been shown in a previous study on dual phase brass [27]. However, it is not clear why the martensite should restrict its slip activity to  $\{110\} \langle 111 \rangle$  glide systems [59–62]. A possible explanation for the observed deviation from typical behaviour might be the influence of the athermal phase transformation on the CRSS of the various slip systems. Speculatively, one could think of elastic internal stresses arising from non-relaxed interstitials that might affect the  $\{112\}$  planes in a different way to the  $\{110\}$  planes.

#### 4. SUMMARY AND CONCLUSIONS

The development of the microstructure and crystallographic texture of a strip cast and of a hot rolled austenitic stainless steel (18 mass% Cr, 8.5 mass% Ni) during cold rolling has been studied. The main results are as follows:

(1) The hot band revealed a homogeneous microstructure and a weak orientation distribution with a texture gradient between the centre and surface layers. This texture inhomogeneity was interpreted in terms of the profile of the shear strains during hot rolling.

(2) The strip cast sample revealed a less

homogeneous microstructure and a weak texture fibre close to  $\{100\} \langle uvw \rangle$ , which was attributed to growth selection.

(3) After cold rolling ( $\geq 60\%$  thickness reduction) both types of sample revealed a strong B and an equal (hot band) or even stronger (strip cast) Goss component. This phenomenon was explained in terms of transformation selection. Based on the results of Goodchild *et al.* [53] it was suggested that the Goss component remained stable whilst the B orientation was unstable with respect to strain induced martensitic transformation.

(4) The rolling texture of the austenite, especially the stabilization of the B orientation, was successfully simulated by using the card glide mechanisms suggested by Hu [31] but with the reinterpretation of Kocks and Necker [32]. The best agreement between experiment and prediction was achieved for simulations in which the ratio of the critical resolved shear stresses (CRSS) for slip in the  $\langle 211 \rangle$  and  $\langle 110 \rangle$  directions was equal to 0.96.

(5) The rolling texture of the martensite revealed both a strong  $\{211\} \langle 011 \rangle$  and a strong  $\{111\} \langle 112 \rangle$  component. The  $\{001\} \langle 110 \rangle$  component was very weak. The basic texture evolution was explained and successfully simulated in terms of the Sachs model. It was shown that the strong  $\{111\} \langle 112 \rangle$  component resulted from the B orientation (austenite) which selectively transformed to the  $\{332\} \langle 113 \rangle$  orientation (martensite). The



latter component was unstable and rotated towards the stable  $\{111\}\langle 112 \rangle$  orientation.

**Acknowledgement**—The author gratefully acknowledges the kind support of the strip casting research group of Krupp-Hoesch Stahl AG (now Krupp-Thyssen Nirosta GmbH).

## REFERENCES

1. K. Ohno, H. Tanaka, T. Sasaki, M. Dubke, H. J. Funk, K. H. Hanke, H. Pfeifer and R. Hentrich, *Proc. Int. Conf. on New Smelting Reduction and Near Net Shape Casting Technologies for Steel*, pp. 14–22. Pohang, South Korea.
2. R. Hentrich, M. Dubke, H. J. Funk, K. H. Hanke, J. Loh and S. Kuhlmann, *Stahl u. Eisen* **111**, 51 (1991).
3. D. Raabe, M. Hölscher, M. Dubke, H. Pfeifer, K. H. Hanke and K. Lücke, *Steel Research* **64**, 359 (1993).
4. D. Raabe, M. Hölscher, M. Dubke and K. Lücke, *Proc. Int. Conf. on Strip Casting, Hot and Cold Working of Stainless Steels*, Quebec, Canada (edited by N. D. Ryan, A. J. Brown and H. J. McQueen), pp. 3–17. The Metallurgical Society of the Canadian Institute of Materials, Montreal, Canada (1993).
5. B. Q. Li, *J. Mater. (JOM)* **47**, 13 (1995).
6. B. Q. Li, *J. Mater. (JOM)* **47**, 29 (1995).
7. D. Raabe, M. Hölscher, F. Reher and K. Lücke, *Scripta metall.* **29**, 113 (1993).
8. D. Raabe, M. Hölscher, M. Dubke, F. Reher and K. Lücke, *Mater. Sci. Forum* **157–162**, 1039 (1994).
9. D. Raabe, *Metall. Mater. Trans. A* **26A**, 991 (1995).
10. D. Raabe, *Mater. Sci. Technol.* **11**, 461 (1995).
11. S. Thiem, W. Löser and M. Jurisch, *Steel Research* **64**, 307 (1993).
12. W. Löser and D. M. Herlach, *Metall. Mater. Trans. A* **23A**, 1585 (1992).
13. K. Shibuya and M. Ozawa, *ISIJ International* **31**, 661 (1991).
14. S. Kiyake, H. Yamane, M. Yukumoto and M. Ozawa, *ISIJ International* **31**, 689 (1991).
15. D. Raabe and K. Lücke, *Mater. Sci. Technol.* **9**, 302 (1993).
16. D. Raabe and K. Lücke, *Scripta metall.* **26**, 1221 (1992).
17. M. Hölscher, D. Raabe and K. Lücke, *Steel Research* **62**, 567 (1991).
18. K. Bethke, M. Hölscher and K. Lücke, *Mater. Sci. Forum* **157–162**, 1137 (1994).
19. D. Raabe, *J. Mater. Sci.* **30**, 47 (1995).
20. T. J. Rickert, *Mater. Sci. Forum* **157–162**, 2017 (1994).
21. S. R. Goodman and H. Hu, *Trans. Metall. Soc. AIME* **230**, 1413 (1964).
22. C. D. Singh, V. Ramaswamy and C. Suryanarayana, *Textures and Microstructures* **13**, 227 (1991).
23. T. G. Smith, *Proc. 5th Int. Conf. on Textures of Materials* (edited by G. Gottstein and K. Lücke). Vol. 2, p. 485. Springer Verlag, Aachen, Germany (1978).
24. C. Donadille, R. Valle, P. Dervin and R. Penelle, *Acta metall.* **37**, 1547 (1989).
25. D. Raabe, in preparation.
26. K. Mäder and E. Hornbogen, *Scripta metall.* **8**, 979 (1974).
27. O. Engler, J. Hirsch and K. Lücke, *Z. Metallkunde* **86**, 465 (1995).
28. U. Schmitter, Diploma Thesis, RWTH Aachen, Institut für Metallkunde und Metallphysik, K. Lücke (1993).
29. D. Raabe, *Acta metall.* **43**, 1023 (1995).
30. U. Schmitter and K. Lücke, in preparation.
31. H. Hu, R. S. Cline, S. R. Goodman, in *Proc. ASM Seminar on Recrystallization, Grain Growth and Textures* (edited by H. Margolin), p. 295. American Society of Metals, Metals Park, Ohio (1966).
32. U. F. Kocks and C. T. Necker, *Proc. 15th RISØ Int. Symp. on Materials Science 'Numerical Prediction of Deformation Processes and the Behaviour of Real Materials'* (edited by S. I. Andersen, J. B. Bilde-Sorensen, T. Lorentzen, O. B. Pedersen and N. J. Sorensen), pp. 45–57. RISØ National Lab., Roskilde, Denmark (1994).
33. L. G. Schulz, *J. appl. Phys.* **20**, 1030 (1949).
34. H. J. Bunge and C. J. Esling, *Physique-Lettr.* **40**, 627 (1979).
35. M. Dahms and H. J. Bunge, *J. appl. Crystallogr.* **22**, 439 (1989).
36. M. Dahms, *Textures and Microstructures* **19**, 169 (1992).
37. H. J. Bunge, *Texture Analysis in Materials Science*. Butterworths, London (1982).
38. D. Raabe, *Textures and Microstructures* **23**, 115 (1995).
39. U. Siegel, H.-J. Spies and H.-J. Eckstein, *Steel Research* **57**, 25 (1986).
40. J. Hirsch and K. Lücke, *Acta metall.* **36**, 2863 (part I), 2883 (part II) (1988).
41. R. E. Schramm and R. P. Reed, *Metall. Trans.* **6A**, 1345 (1975).
42. J. Hirsch, *Hot Deformation of Aluminium Alloys* (edited by T. G. Langdon, M. D. Merchant, J. G. Morris and M. A. Zaidi), pp. 379–385. TMS Aachen, Germany (1991).
43. M. Hölscher, D. Raabe and K. Lücke, *Acta metall.* **42**, 879 (1994).
44. W. Mao, Doctoral Thesis, RWTH Aachen, pp. III–11, 19 and p. III–28 (1988).
45. J. H. Beynon, P. R. Brown, S. I. Mizban, A. R. S. Ponter and C. M. Sellars, in *Computational Techniques for the Prediction of Materials Processes and Defects* (edited by M. Preddeleanu), pp. 19–28. Elsevier, Amsterdam (1987).
46. A. J. McLaren and C. M. Sellars, *Mater. Sci. Technol.* **8**, 1090 (1992).
47. J. Hirsch, E. Nes and K. Lücke, *Acta metall.* **35**, 427 (1987).
48. G. Wassermann, *Z. Metallkunde* **54**, 61 (1963).
49. P. van Houtte, *Acta metall.* **26**, 591 (1978).
50. H. Mecking, *Proc. 6th Int. Conf. on Textures of Materials* (edited by S. Nagashima), p. 53. Iron and Steel Inst. of Japan, Tokyo (1981).
51. I. L. Dillamore and W. T. Roberts, *Metall. Reviews* **10**, 271 (1965).
52. H. R. Wenk, H. J. Bunge, J. Kallend, K. Lücke, S. Matthies, J. Pospiech and P. van Houtte, *Proc. 8th Int. Conf. on Textures of Materials* (edited by J. Kallend and G. Gottstein), p. 17. The Metall. Soc. (1988).
53. D. Goodchild, W. T. Roberts and D. V. Wilson, *Acta metall.* **18**, 1137 (1970).
54. G. E. G. Tucker, *Acta metall.* **12**, 1093 (1964).
55. G. I. Taylor, *J. Inst. Met.* **62**, 307 (1938).
56. H. Honneff and H. Mecking, *Proc. 5th Int. Conf. on Textures of Materials* (edited by G. Gottstein and K. Lücke), p. 265. Springer Verlag (1978), and *Proc. 6th Int. Conf. on Textures of Materials* (edited by S. Nagashima), p. 347. Iron and Steel Inst. of Japan, Tokyo (1981).
57. U. F. Kocks and H. Chandra, *Acta metall.* **30**, 695 (1982).
58. P. van Houtte, *Proc. 6th Int. Conf. on Textures of Materials* (edited by S. Nagashima), p. 428. Iron and Steel Inst. of Japan, Tokyo (1981).
59. D. Raabe, K. Lücke, *Mater. Sci. Forum* **157–162**, 597 (1994).



60. F. Emren, U. von Schlippenbach and K. Lücke, *Acta metall.* **34**, 2015 (1986).
61. D. Raabe, *Mater. Sci. Engng A* **197**, L1–L3, 31 (1995).
62. D. Raabe, *Mater. Sci. Technol.* **11**, 455 (1995).
63. Z. Nishiyama, *Sci. Rep. Inst., Tohoku Univ.* **23**, 638 (1934/1935).
64. G. Wassermann, *Archiv Eisenhüttenwesen* **16**, 647 (1933).
65. G. J. Davies, J. S. Kallend and P. P. Morris, *Acta metall.* **24**, 159 (1976).
66. A. Jones and B. R. Walker, *Metal Sci.* **8**, 394 (1974).
67. R. Ray and J. J. Jonas, *Int. Mat. Rev.* **35**, 1 (1990).